Electrochimica Acta 390 (2021) 138797

Contents lists available at ScienceDirect

Electrochimica Acta

journal homepage: www.elsevier.com/locate/electacta

3D Ta_3N_5 thin film confined-growth Co nanoparticles for efficient bifunction electrolyzed water

Yuanfeng Gao[a], Zhaomin Tong[b], Xiujun Fan[a,c,*]

[a] Institute of Crystalline Materials, Shanxi University, Taiyuan, Shanxi 030006, China
[b] State Key Laboratory of Quantum Optics and Quantum Optics Devices, Institute of Laser Spectroscopy, Shanxi University, Taiyuan, Shanxi 030006, China
[c] Institute of Molecular Science, Shanxi University, Taiyuan, Shanxi 030006, China

ARTICLE INFO

Article history:
Received 2 February 2021
Revised 14 May 2021
Accepted 14 June 2021
Available online 22 June 2021

Keywords:
Bifunctional catalysts
Hydrogen evolution reaction (HER)
Oxygen evolution reaction (OER)
Confined-growth
Ta_3N_5

ABSTRACT

The abundant water resources from the earth are natural feedstocks for the electrolysis of water to produce hydrogen, and there is an urgent need for an efficient and stable catalyst for hydrogen evolution reaction (HER) and oxygen evolution reaction (OER). Exploration of noble-metal-free, highly-efficient and durable bifunctional catalysts for HER and OER remains a challenge. In this work, Co-Ta_3N_5 catalysts were successfully prepared by in situ confined growth of active catalytic species within porous nanofilm using three-dimensional (3D) tantalum nitride (Ta_3N_5) porous nanofilm as templates. After electrochemical testing, we found that Co-Ta_3N_5 nanohybrid exhibits excellent OER and HER performance. Benefiting from the 3D composite nanostructures, the catalysts have excellent electron conduction rates and sufficient active sites, the Co-Ta_3N_5 nanocomposites nitrided at 800 °C exhibits relatively good catalytic activity for HER in acidic (low overpotential of 59.1 mV at 10 mA cm^{-2}, small Tafel slope of 58 mV dec^{-1}) and alkaline (low overpotential of 93 mV at 10 mA cm^{-2}, Tafel slope of 97 mV dec^{-1}) media, respectively. Co-Ta_3N_5-800 also exhibits relatively good catalytic activity for OER with low overpotentials 358 mV at 10 mA cm^{-1} in 1M KOH and the Tafel slope of 58.5 mV dec^{-1}. Additionally, Co-Ta_3N_5-800 possesses excellent catalytic performance, and its catalytic performance with almost no degradation in catalytic performance after severe electrochemical tests, which ascribe to the structure of cobalt nanoparticles that confined-growth in Ta_3N_5 nanotubes. This discovery may pave a new avenue toward the development of robust inexpensive electrocatalysts for OER and HER.

1. Introduction

With the rapid development of the global economy, the demand for energy is also increasing. Resource depletion and environmental issues have been on the forefront of human development due to our over-reliance on fossil fuels such as oil and coal [1]. To cope with these problems, there is an urgent need for alternative energy sources with high energy density and zero pollution, the emergence of hydrogen meets above requirement [2-5]. However, the Earth does not have pure hydrogen, which can only be converted from other hydrogen-containing compounds by conventional methods such as steam reforming and coal gasification, and this process inevitably produces the CO_2 greenhouse gas. Hydrogen produced by electrolysis of water perfectly solves the above problems [5-9]. Firstly, because of the abundance of various types of water on the earth, and secondly, electrolyzed water technology is environmentally friendly and compatible with renewable energy sources such as solar and wind energy. The purpose of preparing a catalyst with high activity and stability is to improve the conversion efficiency between different formats of energy [10-12]. Especially, on earth, there are different water sources with different pH values including seawater, industrial waste water, domestic water. Water sources with different pH values require different catalytic conditions, which will inevitably increase the cost of water electrolysis [13-16]. From this point, the catalyst with good adaptability to electrolysis of water at different pH values is desired [17–21].

At present, noble metals (Pt, RuO_2 and IrO_2) are the state-of-the-art hydrogen evolution reaction (HER) and oxygen evolution reaction (OER) electrocatalysts [8,9], but the biggest drawbacks is expensive and scarce, which limits their large-scale application to industry. Therefore, it is highly necessary to develop an effective, cheap and earth-abundant bifunctional electrocatalyst for OER and HER. Nowadays, various non-noble electrocatalysts have been developed for the HER and OER, including phosphides [22-28], nitrides [29-33], sulfides [34-38], and so forth, but most of them are still subjected to pH conditions. That is, only a few catalysts

* Corresponding author.
E-mail address: fxiujun@gmail.com (X. Fan).

https://doi.org/10.1016/j.electacta.2021.138797
0013-4686/

can exhibit outstanding catalytic HER and OER activities concurrently in a wide range of pH media [39-41], which makes it difficult to improve energy conversion efficiency in some alkaline environments. Compared to other materials, transition metal nitrides (TMNs) has attracted great attention for its high chemical stability, high resistance against corrosion, and low electrical resistance [42-46]. TMNs are promising catalyst substrates and have made great progress in HER and OER in recent years, but there is still room for improvement [47].

In this work, Co-Ta_3N_5 catalysts were successfully prepared by in situ confined growth of active catalytic species within porous nanofilm, which using three-dimensional (3D) tantalum nitride (Ta_3N_5) porous nanofilm as templates. This catalyst exhibits excellent HER catalytic activity under both acidic and basic conditions. This nanohybrid electrocatalyst exhibits exceptional HER activity with the overpotentials as low as 59.1 mV and 93 mV at 10 mA cm^{-2} in 0.5 M H_2SO_4 and 1M KOH electrolytes, respectively. The catalyst also exhibits very low onset potentials with the potentials as low as 10.9 mV and 48.6 mV in 0.5 M H_2SO_4 and 1M KOH electrolytes, respectively. As for the mechanism, Co-Ta_3N_5 hybrid structures provides fully exposed active sites for catalytic reactions, the nitrogen-doped carbon-encapsulated core-shell structure provides desired electron density, which optimizes H desorption strength and enhances water adsorption ability, significantly promoting the intrinsic HER and OER activity.

2. Experimental section

2.1. Synthes is of the Ta_2O_5 films

The 1cm^2 tantalum foil was ultrasonically cleaned with acetone, ethanol, and deionized water to remove the organic matter and impurities on the surface, and then dried with nitrogen. A circular tantalum foil with a diameter of 0.5 cm (0.196 cm^2) was exposed as the anode and a platinum sheet as the cathode was oxidised anodically at 60 V for 15 minutes in a mixed solution of 0.27 mol L^{-1} NH_4F and 15.89 mol L^{-1} H_2SO_4 using a DC regulated power supply. The obtained sample was rinsed with slowly flowing anhydrous ethanol and distilled water, then blown dry with nitrogen to obtain nanoporous tantalum oxide films.

2.2. Synthesis of the Ta_3N_5 films

The Ta_3N_5 films grown on tantalum foil was synthesized from Ta_3O_5 films by a single chemical vapor deposition (CVD) step. Nanoporous tantalum oxide films were a porcelain boat at the middle side of the furnace. The porcelain boat was heated to 800 °C for 1 h under a mixture of argon (Flow rate is 50 sccm) and ammonia (Flow rate is 20 sccm) atmosphere at a total pressure of 0.35 Kpa, and then was cooled to room temperature. The temperature increasing rate is 10 °C min^{-1}.

2.3. Synthesis of the Co-Ta_3N_5 nanohybrid

4-(1H-1,2,4-triazol-1-yl) benzoic acid (tzbc) (0.038 g, 0.2 mmol) and $Co(NO_3)_2$•$6H_2O$ (0.119 g, 0.4 mmol) were dissolved in a solvent mixture of anhydrous ethanol (4 ml) and H_2O (2.5 ml) and then stirred vigorously. The tantalum oxide nanofilms were placed in a cubic copper cage and suspended in a solvent and kept in an air atmosphere for twenty minutes, then the solution and the porous tantalum oxide films were transferred into a Teflon-lined autoclave heated in an oven at 130 °C for 48h. After cooling to room temperature, porous tantalum oxide films were washed by deionised water. The resulting porous tantalum oxide precursors were placed in a porcelain boat in the middle of the furnace. The porcelain boat was heated to 700 °C, 800 °C, 900 °C for 1 h under a mixture of argon (Flow rate is 50 ml/min) and ammonia (Flow rate is 20 ml/min) atmosphere at a total pressure of 0.35 Kpa, and then were cooled to room temperature. The temperature increasing rate is 10 °C min^{-1}. The samples treated at different CVD temperatures were named Co-Ta_3N_5-700, Co-Ta_3N_5-800 and Co-Ta_3N_5-900 respectively.

2.4. Characterization

Powder X-ray diffraction (XRD) data were acquired on a D8 Advance X-ray diffractometer (Germany, Bruckner) with Cu Kα radiation. The transmission electron microscope (TEM) images of samples were measured with a TEM, JEM-2010HR, and high-resolution TEM (HRTEM, 200 kV or 300 kV). The scanning electron microscope (SEM) images of samples were measured with Zeiss Sigma field-emission SEM (FE-SEM, JSM-6700F). The X-ray photoelectron spectroscopy (XPS) spectra were measured on an XPS, PHI 5000 Versa Probe X-ray photoelectron spectrometer. All XPS spectra were corrected using C 1s line at 284.6 eV, and curve fitting and background subtraction were accomplished. The DXR Smart Raman spectrometer of Thermo Fisher Company was used to analyze the structure of the sample, and the excitation wavelength was 532 nm.

2.5. Electrochemical measurements

All electrochemical measurements were performed on a CH Instruments electrochemical workstation (CHI760 Shanghai Chenhua) and based on three electrodes system in electrolyte solution of 0.5 M H_2SO_4 and 1.0 M KOH, the catalysts Co-Ta_3N_5 was used as the working electrode, a carbon rode or platinum wire as counter electrode and saturated calomel electrode as reference electrode. The GC loaded with 20% Pt/C (2.0 mg cm^{-2}) as cathodes under same condition for HER. The whole electrochemical experimengts were executed in 0.5 M H_2SO_4 electrolyte at room temperature. Prior to the measurement, the electrolytes were purged with N_2 gas for 10 min to remove oxygen. The HER performance of each catalysts was investigated using LSV at the scan rate of 5 mV s^{-1}. The stability of catalysts was tested by chronoamperometry and continuous CV cycles. All the data here were collected without iR compensation and converted according to Nernst equation: E(RHE)=E(SCE)+(0.242+0.059pH) V.

3. Results and discussion

The preparation process schematic diagram was showed in **Fig. 1a**. In brief, [$Co(tzbc)_2(H_2O)_4$] crystals were first confined grown in tantalum oxide nanofilm by hydrothermal method, and then nitrided by chemical vapour deposition at high temperature in an Ar/NH_3 atmosphere, nitrogen-doped carbon coated cobalt nanoparticles were reduced in situ and confined inside Ta_3N_5 nanotubes, synthesized a confined-growth Co-Ta_3N_5 catalyst successfully.

Scanning electron microscope (SEM) and Transmission electron microscopy (TEM) were used to observe the morphology of Ta_3N_5 based nanocomposites. As revealed in Fig. 1b, the nanofilm of Co-Ta_3N_5-800 is tightly grown on a metallic tantalum foil substrate and the entire 3D nanofilm consists of numerous stands of Ta_3N_5 nanotubes, which thickness is approximately 7.04 μm. The forest of Ta_3N_5 nanotubes were interconnected by a network of cobalt nanorods in **Fig. 1c**, a special heterostructure that facilitates catalyst stabilisation and charge transfer [48,49]. As revealed in **Fig. 1d**, cobalt nanoparticles are clearly visible inside the Ta_3N_5 nanotubes. The confined-growth [$Co(tzbc)_2(H_2O)_4$] crystals within the nanotubes were annealed at 800°C, the cobalt elements in the [$Co(tzbc)_2(H_2O)_4$] crystals were reduced in situ to

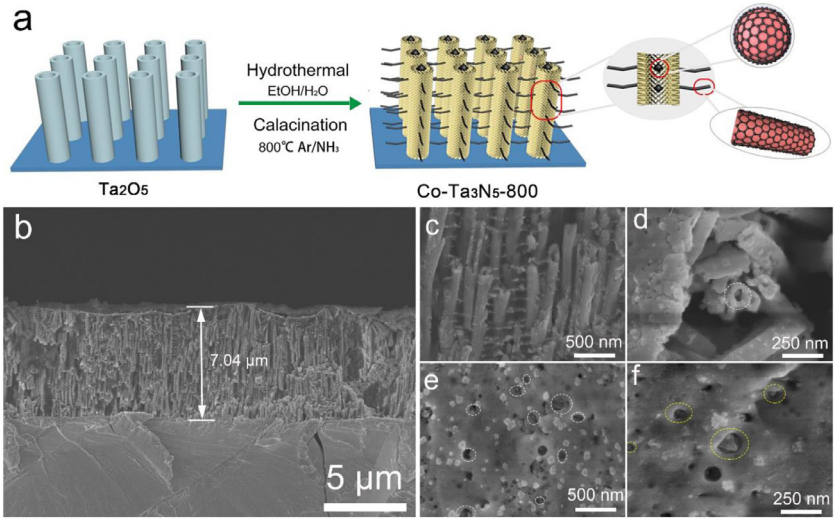

Fig. 1. (a) A schematic diagram showing the synthesis of Co-Ta_3N_5 nanohybrid catalysts. (b) Low-magnification SEM images of the Co-Ta_3N_5-800 nanohybrids formed on the tantalum foil surface. (c,d) High-magnification SEM images of the 3D Co-Ta_3N_5-800. (e,f) High-magnification SEM images of the Co-Ta_3N_5-800 nanofilm surfaces.

metallic cobalt nanoparticles. Because the $[Co(tzbc)_2(H_2O)_4]$ crystals contained a large amount of carbon, the cobalt nanoparticles were completely encapsulated by the carbon layer to form a core-shell structure. Co nanoparticles are also distributed on the surface of Ta_3N_5 nanofilms and within the orifices of the surface (**Fig. 1e-f**). which indicated that the Co nanoparticles are stacked inside the Ta_3N_5 nanotubes and increasing the loading capacity of the Co nanoparticles.

To investigate the effect of nitriding temperature on the morphology of Co-Ta_3N_5 nanocomposites nitrided at different temperatures, SEM and TEM images were used. **Fig S1** shows a sample of Co-Ta_3N_5 nitrided at 700 °C, which revealed a smooth, straight tubular structure, and the pipe wall was connected with short and thick Co nanorods coated with nitrogen-doped carbon. Unlike Co-Ta_3N_5-700, in-depth observations reveal that Co-Ta_3N_5-800 (**Fig. S2**) displays porous hollow Ta_3N_5 nanotubes with long and thin nitrogen-doped carbon-coated Co nanorods in a mesh interlinking the hollow Ta_3N_5 nanotubes. This nanohybrid structure of the Co-Ta_3N_5 has not been reported previously, which is related to the thermal decomposition of the $[Co(tzbc)_2(H_2O)_4]$ crystals that is confined-growth inside the nanofilm. As shown in **Fig S3**, most of the hollowed-out Ta_3N_5 nanotubes in Co-Ta_3N_5-900 were fractured and collapsed due to high temperature, and the Co nanorods between the pipe walls were agglomerated into nanoparticles simultaneously.

The TEM images of Co-Ta_3N_5 samples at different temperatures were characterized. As revealed in **Fig. 2**, it can be determined that as the temperature increases, the smooth Ta_3N_5 nanotubes became rough, and the number of pores gradually increased. The structure of the nanotubes is disrupted at 900 °C (**Fig. 2g-h**), and the cobalt nanoparticles encapsulated by nitrogen-doped carbon layers also agglomerate with increasing temperature. The particle size of cobalt nanoparticles was 30.32 nm at 700 °C (**Fig. 2c**) and 52.66 nm at 900 °C (**Fig. 2i**), respectively. The particle size of cobalt nanoparticles was 46.71 nm at 800 °C (**Fig. 2f**), which can be perfectly confined within the tantalum nitride nanopores, greatly enhancing the stability of the composite material. Compared with the other two samples, Co-Ta_3N_5-800 has a special hollow-out nanotube structure, which greatly enhances the specific surface area of the tantalum nitride nano-film substrate, exposing more active sites for proton adsorption and desorption [17,50]. On the other hand, this porous structure also facilitates the direct penetration of the electrolyte and has stronger hydrophilicity, which is consistent

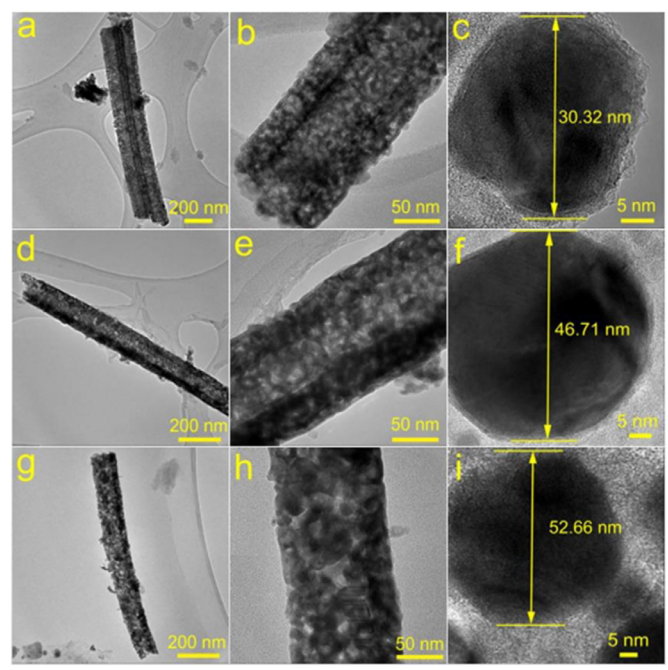

Fig. 2. TEM images of the Co-Ta_3N_5 nanohybrids with different annealing temperature. (a-c) 700 °C; (d-f) 800 °C; (g-i) 900 °C.

with the contact angle information shown in **Fig. S4**. The porous structure enables the active site to contact the electrolyte directly and quickly, which greatly improves the performance of electrocatalytic water decomposition of the whole composite material.

To further investigate the microscopic morphology of Ta_3N_5 nanotubes and nitrogen-doped carbon-coated cobalt nanoparticles, high-resolution TEM was used to characterize the Co-Ta_3N_5-800 samples. As shown in **Fig. 3a-b**, many bright holes (dashed yellow circles) can be seen on the surface of the tantalum nitride nanotubes, consistent with the SEM observation. The diameter of the holes on the nanotube are approximately 5.9 nm, which are favorable for the electrolyte quickly penetrate through the thick Ta_3N_5 electrodes. The lattice spacing of Ta_3N_5 measured in the area selected by the yellow wireframe is 0.53 nm (**Fig. 3c**), which corresponds to the (002) crystal plane of Ta_3N_5. The pore diameter of the Ta_3N_5 nanotube is about 47 nm with wall thickness of approx-

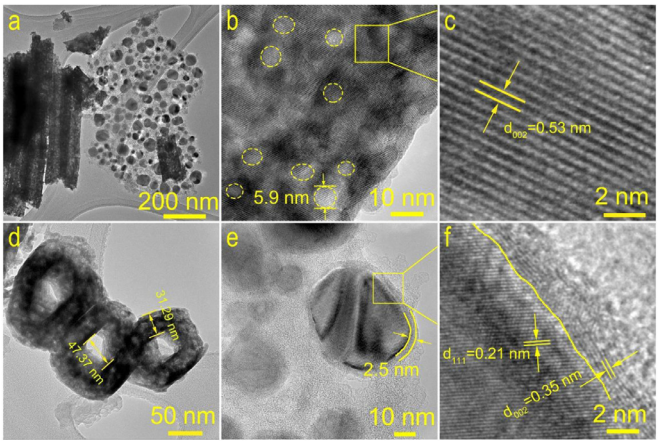

Fig. 3. (a) The TEM image of Co-Ta_3N_5-800. (b-d) HRTEM image of Ta_3N_5 nanotubes in Co-Ta_3N_5-800 samples. (e,f) HRTEM image of nitrogen-doped carbon-coated cobalt nanoparticles in Co-Ta_3N_5-800 nanotubes.

imately 31 nm (**Fig. 3d**). The thick wall still maintains good mechanical stability even though there are many hollowed-out pores on surface of the Ta_3N_5 nanotube. The Co nanoparticles shown in **Fig. 3e** is completely encapsulated by a carbon layer with a thickness of about 2.5 nm at the edges. It is also observed in **Fig. 3f** that the interlayer spacing of the graphite (002) surface has expanded from 0.34 nm to 0.35 nm, which should be attributed to nitrogen doped [51]. The lattice spacing of Co near the carbon layer is 0.21 nm, which corresponds to the (111) crystal plane of the metallic cobalt [52], indicating that the Co nanoparticles are highly crystalline, consistent with the XRD results (**Fig. 4a**). Furthermore, the high annular dark-field scanning TEM (HAADF-STEM) image and corresponding elemental mapping reveal the uniform distribution of Co, C, Ta and N elements within the whole nanotube (**Fig. S5**). It is noteworthy that the nitrogen-doped carbon-coated Co nanoparticles match the size of the Ta_3N_5 nanotubes, indicating that the confined-growth Co nanocomposite catalyst was successfully synthesized.

Powder X-ray diffraction (XRD) was employed to further determine the chemical and phase compositions. The three peaks appearing at 38.4, 55.5 and 69.5°, as depicted in **Fig. 4a**, are correspond to the (110), (220) and (210) crystal faces of metallic tantalum (JCPDS No.04-0788). The five peaks of Ta_3N_5 was located at 17.2, 24.4, 25.9, 30.1 and 44.9°, which correspond to the (002), (110), (111), (025) and (510) crystal faces of Ta_3N_5 (JCPDS No.19-1291), respectively [53]. The typical (002) peak of Ta_3N_5 was located at 17.2°, indicating an interplanar spacing that is 0.55 nm, which is similar to the lattice spacing of Ta_3N_5 (0.53 nm) observed in TEM image (**Fig. 3c**). The XRD pattern (**Fig. 4a**) of Ta_3N_5 and Co-Ta_3N_5 show no significant difference except for some minor changes, and the two major peaks located at 44.2° and 51.5° (indicated by α) are characteristic of metallic Co (111) and (200) (JCPDS no.15-0806), respectively [54]. indicating that the Co^{2+} in the cobalt nanocrystals $[Co(tzbc)_2(H_2O)_4]$ has been reduced to single crystal cobalt. The typical (111) peak of Co was located at 44.2°, indicating an interplanar spacing that is 0.22 nm, which is similar to the lattice spacing observed from TEM image (0.21 nm, **Fig. 3f**). It is worth noting that no characteristic peaks for the C element are found in **Fig. 4a**.

To further demonstrate that the cobalt nanoparticles are coated with carbon after annealing, the Raman and XPS characterization methods were employed. As shown in **Fig. 4b**, both Co-Ta_3N_5-800 and Ta_3N_5 samples shows the same vibration characteristic peaks of Ta_3N_5 in the range of 100-1000 cm^{-1} [55]. The Raman spectrum of the Co-Ta_3N_5-800 sample was magnified at 1350 cm^{-1} and 1580 cm^{-1} (the inset of **Fig. 4b**), and two weak vibration peaks can be observed corresponding to the D band (amorphous) and G band (graphitic) of the carbon material [56], which indicate that the sample Co-Ta_3N_5-800 is doped with a small amount of carbon from the decomposition of $[Co(tzbc)_2(H_2O)_4]$ crystals. Combined with the previous TEM characterization, it is known that the carbon layers encapsulating the cobalt nanoparticles are graphenes. According to previous reports, carbon can improve the conductivity of the sample and reduce the resistance of charge transfer [57]. Cobalt metal as a single crystal has no molecular bonds and therefore no Raman vibrational modes.

In order to further analyze the chemical composition, atomic valence and composite structure, X-ray photoelectron spectroscopy (XPS) measurements were performed. The XPS survey scan

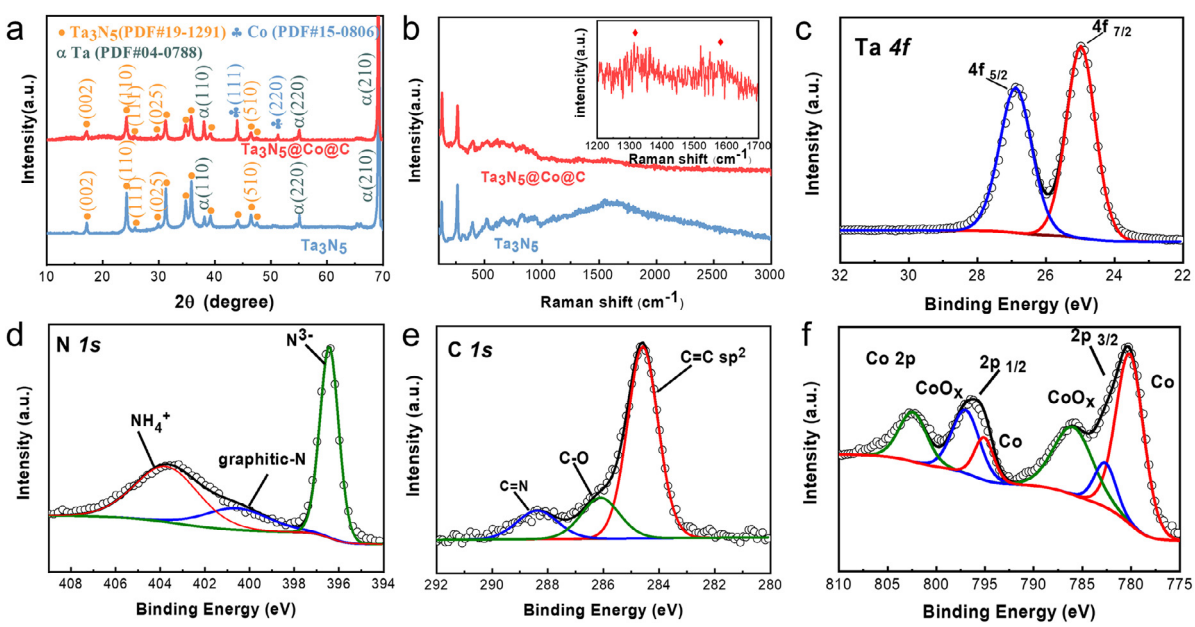

Fig. 4. (a) XRD patterns of samples Co-Ta_3N_5-800and Ta_3N_5. (b) Raman spectra of samples Co-Ta_3N_5-800 and Ta_3N_5. (c) Ta 4f spectrum of Co-Ta_3N_5-800. (d) N 1s spectrum of Co-Ta_3N_5-800. (e) C 1s spectrum of Co-Ta_3N_5-800. (f) Co 2p spectrum of Co-Ta_3N_5-800.

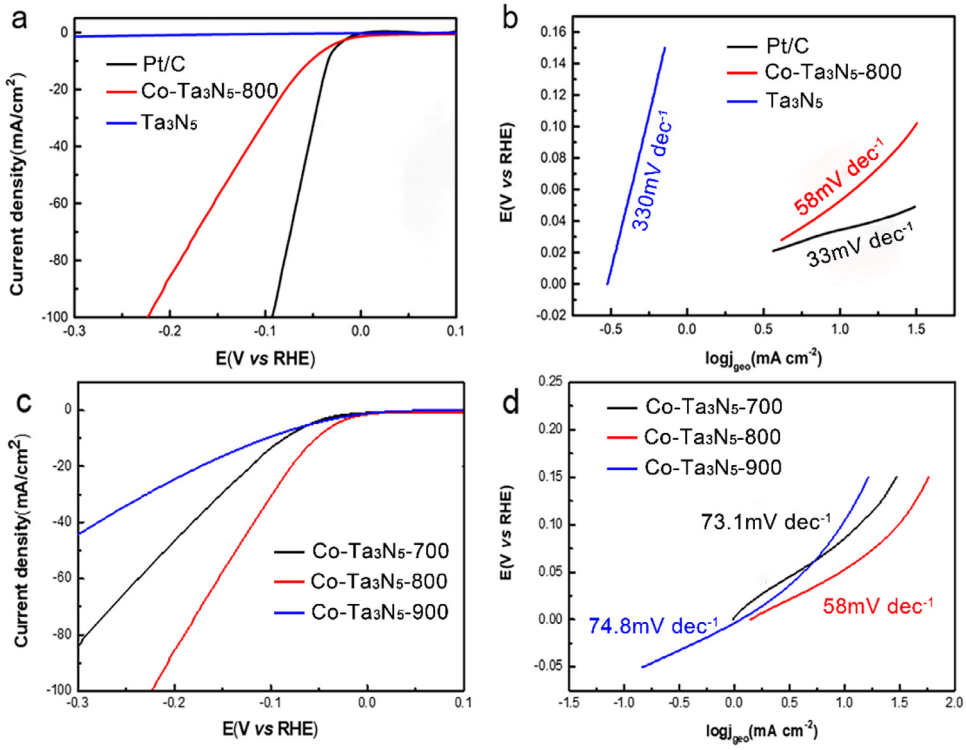

Fig. 5. Hydrogen evolution catalysis in 0.5 M H_2SO_4. (a) The polarization curves of Co-Ta_3N_5-800, Ta_3N_5, and Pt/C. (b) Tafel slope of Co-Ta_3N_5-800, Ta_3N_5, and Pt/C. (c) The polarization curves Co-Ta_3N_5-700, Co-Ta_3N_5-800, and Co-Ta_3N_5-900. (d) Tafel slope of Co-Ta_3N_5-700, Co-Ta_3N_5-800, and Co-Ta_3N_5-900.

(**Fig. S6**) reveal the presence of Co, Ta, N, C and O elements in the Co-Ta_3N_5-800 samples, which also confirms the presence of graphenes in the samples. As shown in **Fig. 4c**, the Ta 4f spectrum of Co-Ta_3N_5-800 nanohybrid can be deconvoluted into two main components appearing at 24.9 and 26.9 eV, which are corresponding to Ta $4f^{7/2}$ and Ta $4f^{5/2}$ spin orbits, indicating the formation of Ta_3N_5 [58,59]. The N 1s spectrum (**Fig. 4d**) of the Co-Ta_3N_5-800 sample can be divided into three peaks at 396.4, 400.8 and 404.1 eV, corresponding to N^{3-} and nitrogen in graphene and free nitrogen, respectively [59-61]. This phenomenon shows that there are two kinds of ambient environment for the N element in the sample, one is N^{3-} in Ta_3N_5; the other is graphitic nitrogen, which is derived from high-temperature annealed $[Co(tzbc)_2(H_2O)_4]$ crystals. The Co 2p spectra (**Fig. 4f**) shows the Co $2p^{3/2}$ and Co $2p^{1/2}$ orbitals of Co-Ta_3N_5-800, located at 780.8 and 795.2 eV, respectively [62]. As shown in **Fig. 4f**, the Co $2p^{3/2}$ spectrum of Co-Ta_3N_5-800 nanohybrid can be deconvoluted into three main components appearing at 780.0, 781.1 and 786 eV, which are corresponding to Co, CoO_x and satellite peaks [63]. The presence of metallic Co confirms the reduction of Co^{2+} to metallic Co during the annealing process, which is ascribed to the thermal decomposition of 4-(1H-1,2,4-triazol-1-yl) benzoic acid. Moreover, the C 1s spectrum of high-resolution XPS can be divided into three types of carbon compositions appearing at 284.5, 286.1 and 288.1 eV (**Fig. 3e**), which are corresponding to C=C, C-O and C=N, respectively [60]. The carbon in the sample is dominated by graphitic carbon layer due to the favorable position of C=C bond and a small amount of N doping. As previously reported, a high N content may hinder the crystallinity of carbon, which is in good agreement with our observation that a relatively lower N content in graphene layers [64]. The N doping provides impurity energy levels for nanohybrid materials, and then adjusts the fermi energy level to shift in a favorable direction [41]. The electronic filling state changes, which affects and optimizes the electronic structure of Co-Ta_3N_5-800. Thus, the XRD pattern, Raman spectrum and XPS analysis further corroborate the formation of a Co-Ta_3N_5 nanohybrid structure, consistent with the SEM and TEM observations.

To investigate the effects of the N-doped carbon-coated cobalt nanoparticles on the HER electrocatalytic behavior of our Co-Ta_3N_5 nanohybrid, we carried out linear sweep voltammetry (LSV) measurements in 0.5 M H_2SO_4, and all polarization curves in the article are without iR corrected. As a benchmark, we have also characterized the catalytic performance of commercial Pt/C, which exhibited excellent HER overpotential. The polarization curves shown in **Fig. 5a** and **c** suggest that the catalytic activity of the Co-Ta_3N_5-800 nanohybrid electrode is superior to other non-noble reference electrocatalysts in the whole potential range. Interestingly, the Ta_3N_5 substrate does not exhibit catalytic activity, indicating that the active component is carbon-coated cobalt nanoparticles rather than the Ta_3N_5 substrate. As expected, the Co-Ta_3N_5-800 displayedthe best performance compared to that of Co-Ta_3N_5-900 or Co-Ta_3N_5-700 with the overpotential of 59.1 mV at 10 mA cm^{-2} and onset potential of 10.9 mV (**Fig. S7**), but still inferior to the Pt catalyst. To figure out why this structured nanohybrid catalyst possesses such excellent HER performance in 0.5 M H_2SO_4, we measured the electrochemical impedance spectra (EIS) of Co-Ta_3N_5-800, Ta_3N_5, and Pt/C. Co-Ta_3N_5-800 electrode has the lower charge-transfer resistance to Ta_3N_5 in **Fig. S8**, meaning much faster electrode kinetics of this nanohybrid electrode relative to Ta_3N_5. The cobalt nanorods link the nanotube arrays, which is equivalent to establishing a fast channel for electrons to facilitate the transfer of electrons in the catalyst. This explanation seems to be consistent with the experimental results. In particular, to further present the superior catalytic performance of this Co-Ta_3N_5-800 nanohybrid, we briefly compared its overpotentials at 10 mA cm^{-2} (η_{10}) and Tafel slope with other available non-noble metal electrocatalysts. It is worth noting that the electrocatalytic performance of Co-Ta_3N_5-800 is much better than many other efficient inexpensive electrocatalysts reported recently (**Fig. S9, Table S2** in the Supporting Information).

To predict the intrinsic catalytic reaction kinetics of the sample, the Tafel slope was derived from the corresponding polarization curve using the Tafel formula ($\boldsymbol{\eta} = \mathbf{a} + \mathbf{b} \log \boldsymbol{j}$, where $\boldsymbol{b}$ is the Tafel slope, and $\boldsymbol{j}$ is the current density). A lower Tafel slope indicates more efficient hydrogen reaction evolution dynamics, meaning that increasing the same current density requires smaller overpotentials. As shown in **Fig. 5b-d**, Co-Ta_3N_5-800 delivered a small Tafel slope of 58 mV dec^{-1}, close to that for the commercially available Pt/C catalyst (33.1 mV dec^{-1}), which was lower than Co-Ta_3N_5-900 (74.8 mV dec^{-1}) and Co-Ta_3N_5-700 (73.1 mV dec^{-1}), indicating favorable HER activity. It is well known that under a specific set of conditions, the HER mechanism is divided into two steps in acidic solution, which are electrochemical adsorption process (Volmer) and desorption process (Heyrovsky or Tafel). Generally, a Tafel slope of 120 mV dec^{-1} indicates that the Volmer step is the rate-determining step:

$$H^- + e^- + * \rightarrow *H_{ads}$$

This step is followed by either an electrochemical desorption step (Heyrovsky reaction, Tafel slope is 40 mV dec^{-1}),

$$H^- + e^- + * + *H_{ads} \rightarrow H_2 + 2*$$

or a recombination step (Tafel reaction, Tafel slope is 30 mV dec^{-1}),

$$*H_{ads} + *H_{ads} \rightarrow H_2 + 2*$$

The rate-determining step of Pt/C follows the Volmer-Tafel mechanism in 0.5 M H_2SO_4 solution according to the literature [65]. The Tafel slope of Co-Ta_3N_5-900 and Co-Ta_3N_5-700 increased to 74.8 mV dec^{-1} and 73.1 mV dec^{-1} with the change of annealing temperature (**Fig. S7**), all of them indicated a tendency to limit the absorption of H^+ on active sites (Volmer Step). The slope of Co-Ta_3N_5-800 (58 mV dec^{-1}) implies that the reaction mechanism is the Volmer-Heyrovsky mechanism in the HER, in which the rate-determining step is the desorption process and the reaction kinetics is optimized. According to the characterization results, we know that the annealing temperature has a huge impact on the morphology of the electrocatalyst, which includes the size of the carbon-coated cobalt nanoparticles and the degree of hollowing of the Ta_3N_5 nanotubes, profoundly affecting the HER activity of the catalyst, just as the excellent catalytic activity of Co-Ta_3N_5-800 originates from the right degree of hollowing and the size of carbon-coated cobalt nanoparticles.

To further reveal the essence of the superb activity of this Co-Ta_3N_5-800 nanohybrid, electrochemically active surface area ($EASA = SC_{dl}/C_S$, where S is 1cm^2, and C_S for the Tantalum foil) measurements were performed to determine the active surface area of the catalysts. As displayed in **Fig. S10**, double-layer capacitance (C_{dl}) was calculated by cyclic voltammetric (CV) curves and measured under the non-Faraday voltage interval, and the number of electrochemically active sites was estimated by C_{dl}. The Co-Ta_3N_5-800 catalyst afforded a calculated C_{dl} value of 11.02 mF cm^{-2}, significantly larger than that of the Ta_3N_5. The estimated ECSA value of Co-Ta_3N_5-800 was 275.5 cm^2, indicating the number of active sites has drastically increased, which is attributed to the porous structure of Co-Ta_3N_5-800 nanotubes. Another important performance index to evaluate the electrocatalyst is the long-term electrochemical durability. Noticeably, this nanohybrid catalyst exhibited outstanding electrochemical stability in the acid medium as proven by negligible decay of the overpotentials with time increas-

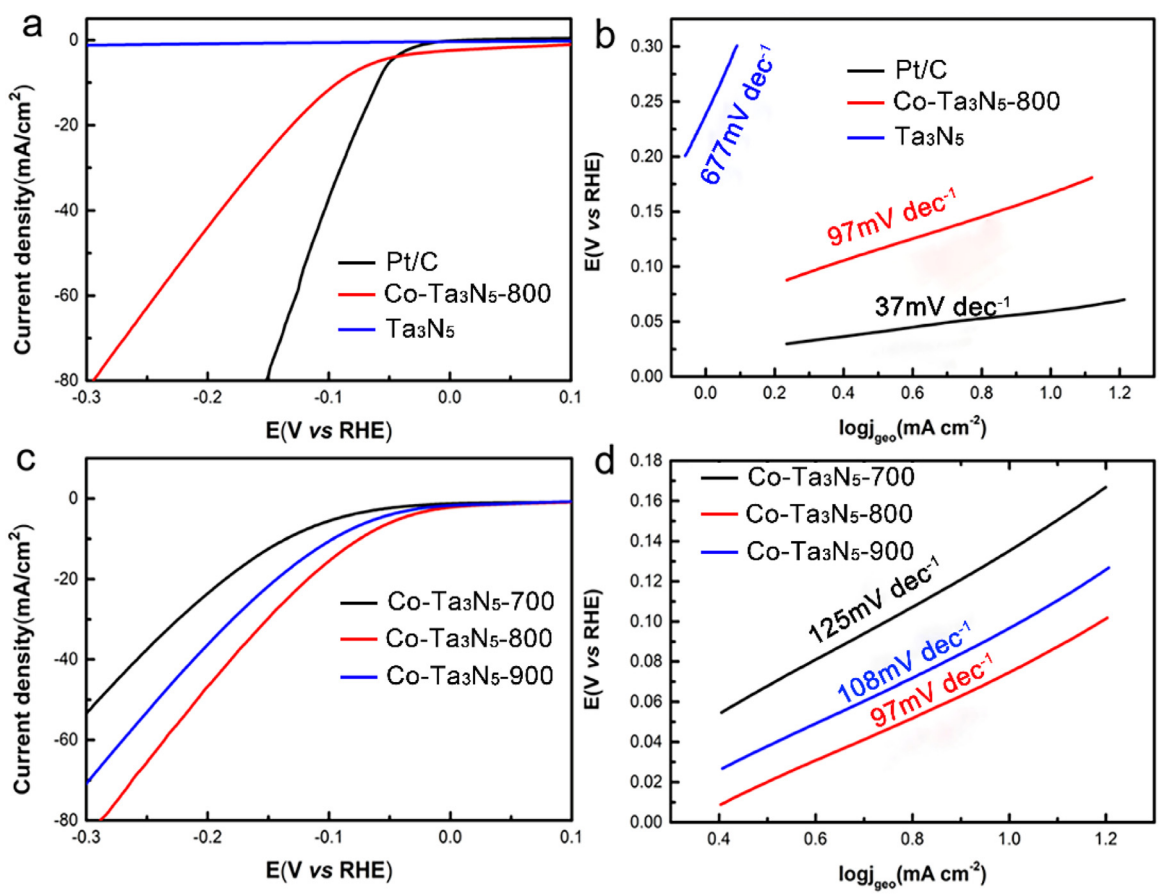

Fig. 6. Hydrogen evolution catalysis in 1 M KOH. (a) The polarization curves of Co-Ta_3N_5-800, Ta_3N_5, and Pt/C. (b) Tafel slope of Co-Ta_3N_5-800, Ta_3N_5, and Pt/C. (c) The polarization curves Co-Ta_3N_5-700, Co-Ta_3N_5-800, and Co-Ta_3N_5-900. (d) Tafel slope of Co-Ta_3N_5-700, Co-Ta_3N_5-800, and Co-Ta_3N_5-900.

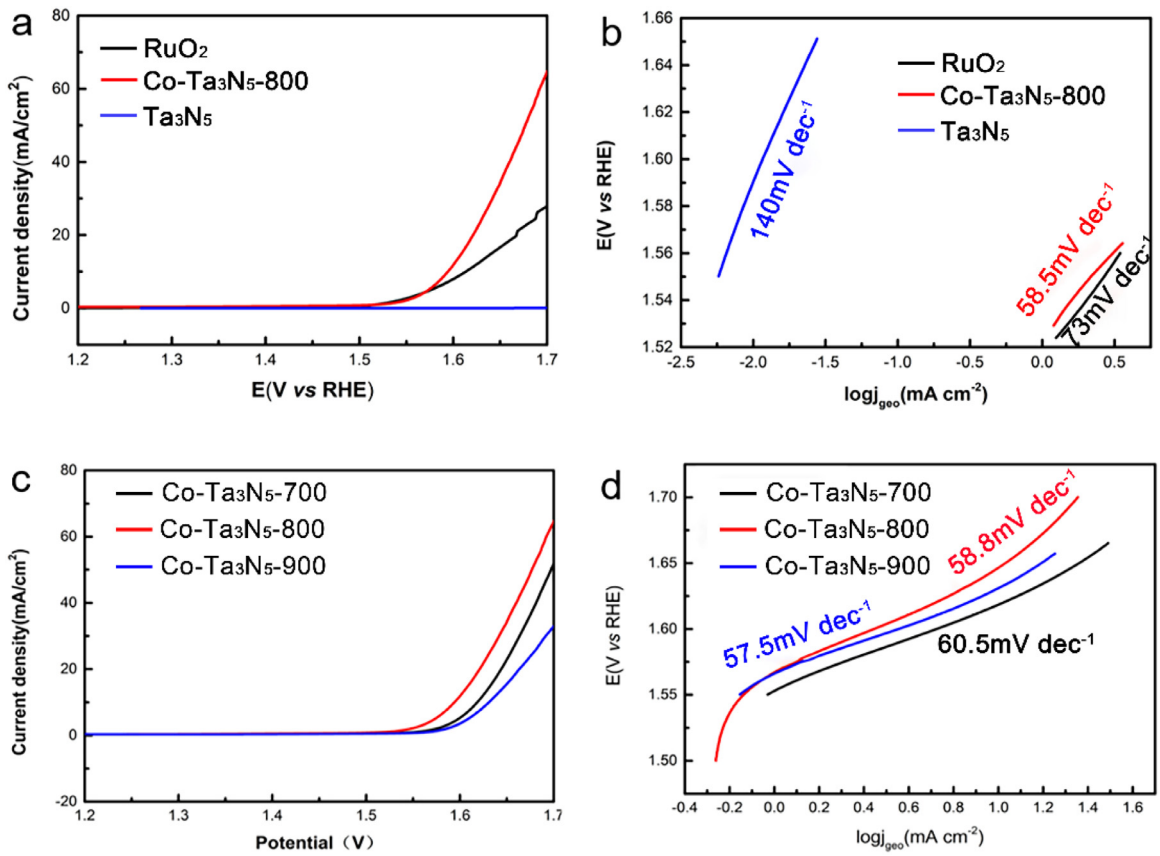

Fig. 7. Oxygen evolution catalysis in 1 M KOH. (a) The polarization curves of Co-Ta_3N_5-800, Ta_3N_5, and Pt/C. (b) Tafel slope of Co-Ta_3N_5-800, Ta_3N_5, and Pt/C. (c) The polarization curves Co-Ta_3N_5-700, Co-Ta_3N_5-800, and Co-Ta_3N_5-900. (d) Tafel slope of Co-Ta_3N_5-700, Co-Ta_3N_5-800, and Co-Ta_3N_5-900.

ing (**Fig. S11**), and the coincident polarization curves between the initial and 3000 cycles. To exclude interference from the platinum electrode, the LSV polarisation curves before and after replacing the platinum counter electrode with a graphite electrode overlap exactly (**Fig. S11 b**), indicating that our test results are true and reliable. In addition, the SEM characterization and Raman spectrum of the Co-Ta_3N_5-800 sample after a long time of testing by the timed current method is shown in **Fig. S12**. After a long period of electrochemical testing, only the cobalt nanoparticles physically adsorbed on the surface of the Ta_3N_5 nanofilm fell off. The Raman spectra before and after the durability test did not change significantly, especially the inset in **Fig. S12c**, which shows that the nitrogen-doped carbon-coated cobalt nanoparticles confined-growth in the Ta_3N_5 is intact. Thus, these observations clearly confirm the superior and durable catalytic activity of this nanohybrid electrode in acidic electrolytes.

The HER performances in 1M KOH electrolyte of the electrocatalysts were also characterized. As shown in **Fig. 6a-b**, Co-Ta_3N_5-800 exhibits excellent catalytic performance, with the low overpotentials of 93 mV for η_{10}, which is closer than that of Pt/C (57.4 mV), and far lower than that of Ta_3N_5 (very large). Next, the Co-Ta_3N_5-800 showed the best performance compared to Co-Ta_3N_5-900 and Co-Ta_3N_5-700 with the overpotential of 93 mV for η_{10} and onset potential of 20.8 mV (**Fig. 6c** and **Fig. S13a**), but still inferior to the Pt catalyst. We measured the electrochemical impedance spectra of Co-Ta_3N_5-800, Ta_3N_5, and Pt/C in 1 M KOH, Co-Ta_3N_5-800 shows the lower charge-transfer resistance to Ta_3N_5 in **Fig. S14**, meaning much faster electrode kinetics of this nanohybrid electrode relative to Ta_3N_5. In particular, to further present the superior catalytic performance of this Co-Ta_3N_5-800 nanohybrid, we have made simple comparison with other available non-noble electrocatalysts on the overpotentials at 10 mA cm^{-2} and Tafel slope. It is worth noting that the electrocatalytic performance of Co-Ta_3N_5-800 outperforming most of the non-noble electrocatalysts tested in basic media reported recently (**Fig. S15, Table S3**). The Tafel slope of Co-Ta_3N_5-900 and Ta_3N_5@C@Co-700 increased to 125 mV dec^{-1} and 108 mV dec^{-1} with the change of annealing temperature (**Fig. 6d** and **Fig. S13 b**), all of them indicated a tendency to suppress the absorption of H^+ on active sites (Volmer Step). As shown in **Fig. 6d**, the slope of Co-Ta_3N_5-800 (97 mV dec^{-1}) implies that the reaction mechanism is the Volmer-Heyrovsky mechanism in the HER, which rate-determining step is the desorption process and the reaction kinetics is optimized. The calculated C_{dl} of Co-Ta_3N_5-800 was 9.49 mF cm^{-2} illustrated in **Fig. S16**, indicating a larger active surface area [66]. Finally, continuous cycling tests and time-dependent current response indicate the superb long-term durability of Co-Ta_3N_5-800 toward HER in alkaline media (**Fig. S17**). Additionally, the SEM characterization and Raman spectrum of the Co-Ta_3N_5-800 sample after a long time testing by the timed current method is shown in **Fig. S18**, suggesting its great potential for commercial alkaline water electrolyzers. In conclusion, these results provide strong evidence of the exceptional H_2-evolving efficiency of our Co-Ta_3N_5-800 catalyst in alkaline media.

To further explore the catalytic properties of Co-Ta_3N_5 composites, the OER performances in 1M KOH electrolyte of the electrocatalysts were also characterized. Impressively, we found that the Co-Ta_3N_5-800 also behaves as an excellent OER electrocatalyst. As clearly given in **Fig. 7a-b**, the as-prepared Co-Ta_3N_5-800 still exhibits much better OER activity than those of Ta_3N_5 and commercial RuO_2 in 1.0 M KOH solutions, which can deliver a smaller OER overpotential (**Table. S1**). Moreover, the Co-Ta_3N_5-800 showed the best performance compared to Co-Ta_3N_5-900 and Co-Ta_3N_5-700

with a smallest overpotential of 357 mV at 10 mA cm^{-2} (**Fig. 7c**). Compared to Co-Ta_3N_5-900 and Co-Ta_3N_5-700, Co-Ta_3N_5-800 has a lower onset potential and Tafel slope (**Fig. 7d**), indicating faster reaction kinetics. We measured the EIS of Co-Ta_3N_5-800, Ta_3N_5, and RuO_2 in 1 M KOH, Co-Ta_3N_5-800 showed the lower charge-transfer resistance to Ta_3N_5 in **Fig. S19**, meaning much faster electrode kinetics of this nanohybrid electrode relative to Ta_3N_5. Continuous cycling tests and time-dependent current response indicate the superb long-term durability of Co-Ta_3N_5-800 toward OER in alkaline media (**Fig. S20**). Additionally, the Raman spectrum of the Co-Ta_3N_5-800 sample after a long time testing by the timed current method is shown in **Fig. S20**, suggesting its great potential for commercial alkaline water electrolyzers. Such excellent catalytic performance may be attributed to the intact nanocomposite structure at 800°C annealing temperature. It is worth noting that the electrocatalytic performance of Co-Ta_3N_5-800 outperforming most of the non-noble electrocatalysts tested in basic media reported recently (**Table S4**).

Considering the outstanding catalytic performance of Co-Ta_3N_5-800 catalysts for HER and OER, we further investigated the overall seawater splitting performance by integrating the two catalysts into a two-electrode alkaline electrolyzer (without a diaphragm or membrane), in which Co-Ta_3N_5-800 is used as the anode for OER and Co-Ta_3N_5-800 as the cathode for HER. Remarkably, this electrolyzer shows excellent overall seawater splitting activity in the alkaline electrolytes. As displayed in **Fig. S21**, at room temperature (25 °C), the cell voltages needed to produce a current density of 10 mA cm^{-2} are as low as 1.621 in 1M KOH electrolytes. Such performance even outperforms that of most non-noble metal catalysts for alkaline freshwater splitting, as well as that of the benchmark of Pt/C and IrO_2 catalysts in 1M KOH. The excellent pH-universal activity and stability of overall water splitting make Co-Ta_3N_5-800 as a potential candidate for practical water electrolysis applications with satisfactory operability, safety, and environmental friendliness.

According to all the above observations, the excellent electrochemical performance of the Co-Ta_3N_5-800 catalyst can be traced back to the following aspects. Firstly, the Co-Ta_3N_5-800 catalyst has a large number of active sites ascribe to its unique structure, that is, the thin film substrate composed of porous Ta_3N_5 nanotubes provides a large number of hydrogen desorption sites, and the free energy of hydrogen adsorption (ΔG_{H^*}) tends to 0. The active sites of cobalt nanoparticles confined-growth inside Ta_3N_5 nanotubes, which were not agglomerated and dispersed due to spatial constraints, thus more effective electrochemical active sites are exposed. Secondly, the outstanding electrical conductivity of Co-Ta_3N_5-800 originates from the fact that nitrogen-doped carbon-coated cobalt nanowires linked to Ta_3N_5 nanotubes form a nanotubular forest, which greatly increases the rate of electron shuttling through the forest and structural stability, and the N doping optimizes the electronic structure of the carbon layer, reducing the resistance to electron transfer. Finally, the nitrogen-doped carbon-encapsulated core-shell structure prevents catalyst deactivation by avoiding direct contact with the electrolyte solution, and the cobalt nanoparticles are anchored inside the nanotubes and will not fall off even after a severe electrochemical process. Both of these two critical points are the reasons for the long electrochemical lifetime of Co-Ta_3N_5-800. Thus, the Co-Ta_3N_5-800 catalysts with a unique structure can exhibit excellent HER performance in acidic and alkaline electrolytes.

4. Conclusion

In conclusion, we have successfully developed an efficient and durable Co-Ta_3N_5 nanohybrid electrocatalyst for hydrogen evolution in acidic and alkaline electrolytes. The Co-Ta_3N_5-800 nanohybrid exhibits outstanding performance toward hydrogen evolution characteristic of the overpotentials 59.1 and 93 mV at 10 mA cm^{-2} in acidic and alkaline solutions, respectively. Co-Ta_3N_5-800 also exhibits relatively excellent catalytic activity for OER with low overpotentials 358 mV at 10 mA cm^{-1} in 1M KOH. Such excellent catalytic performance is probably arisen from large surface area and good conductivity of the Co-Ta_3N_5-800, and the strong synergistic effects between porous nano-Ta_3N_5 film and nitrogen-doped carbon-coated cobalt nanoparticles. The outstanding HER and OER catalytic performance of Co-Ta_3N_5-800 has surpassed that of most current cobalt-containing catalysts and possesses excellent electrochemical stability. We believe that this unique structure provides a new strategy for the preparation of highly efficient non-noble metal bifunctional catalysts.

Declaration of Competing Interest

We declare that we have no financial and personal relationships with other people or organizations that can inappropriately influence our work, there is no professional or other personal interest of any nature or kind in any product, service and/or company that could be construed as influencing the position presented in, or the review of, the manuscript entitled.

Credit authorship contribution statement

Yuanfeng Gao: Writing – original draft, Conceptualization. **Zhaomin Tong:** Writing – review & editing, Conceptualization. **Xiujun Fan:** Writing – review & editing, Conceptualization.

Acknowledgements

The authors acknowledge the Natural Science Foundation of Excellent Young Scholars for Shanxi Province (201901D211198), the Program for the Outstanding Innovative Teams of Higher Learning Institutions of Shanxi (OIT, No. 231544901002), and the Fund for Shanxi "1331" Project for Featured Discipline of Chemistry in SXNU for finance support of this research.

Supplementary materials

Supplementary material associated with this article can be found, in the online version, at doi:10.1016/j.electacta.2021.138797.

References

[1] L. Yang, Z. Liu, S. Zhu, L. Feng, W. Xing, Ni-based layered double hydroxide catalysts for oxygen evolution reaction, Mater. Today Phys. 16 (2021) 100292, doi:10.1016/j.mtphys.2020.100292.
[2] G. Glenk, S. Reichelstein, Economics of converting renewable power to hydrogen, Nat. Energy 4 (2019) 216–222, doi:10.1038/s41560-019-0326-1.
[3] B. Tanç, H.T. Arat, E. Baltacıoğlu, K. Aydın, Overview of the next quarter century vision of hydrogen fuel cell electric vehicles, Int. J. Hydrog. Energy 44 (2019) 10120–10128, doi:10.1016/j.ijhydene.2018.10.112.
[4] M.W. Kanan, D.G. Nocera, In situ formation of an oxygen-evolving catalyst in neutral water containing phosphate and Co^{2+}, Science 321 (2008) 1072, doi:10.1126/science.1162018.
[5] J.-Y. Zhang, T. He, M. Wang, R. Qi, Y. Yan, Z. Dong, H. Liu, H. Wang, B.Y. Xia, Energy-saving hydrogen production coupling urea oxidation over a bifunctional nickel-molybdenum nanotube array, Nano Energy 60 (2019) 894–902, doi:10.1016/j.nanoen.2019.04.035.
[6] F. Wang, Y. Li, T.A. Shifa, K. Liu, F. Wang, Z. Wang, P. Xu, Q. Wang, J. He, Selenium-enriched nickel selenide nanosheets as a robust electrocatalyst for hydrogen generation, Angew. Chem. Int. Ed. 55 (2016) 6919–6924, doi:10.1002/anie.201602802.
[7] L. Huang, D. Chen, G. Luo, Y.-R. Lu, C. Chen, Y. Zou, C.-L. Dong, Y. Li, S. Wang, Zirconium-regulation-induced bifunctionality in 3D cobalt–iron oxide nanosheets for overall water splitting, Adv. Mater. 31 (2019) 1901439, doi:10.1002/adma.201901439.
[8] X. Ren, Q. Lv, L. Liu, B. Liu, Y. Wang, A. Liu, G. Wu, Current progress of Pt and Pt-based electrocatalysts used for fuel cells, Sustain. Energy Fuels 4 (2020) 15–30, doi:10.1039/C9SE00460B.

[9] X.H. Chen, Q. Zhang, L.L. Wu, L. Shen, H.C. Fu, J. Luo, X.L. Li, J.L. Lei, H.Q. Luo, N.B. Li, Regulation of the electronic structure of Co_4N with novel Nb to form hierarchical porous nanosheets for electrocatalytic overall water splitting, Mater. Today Phys. 15 (2020) 100268, doi:10.1016/j.mtphys.2020.100268.
[10] F. Yu, L. Yu, I.K. Mishra, Y. Yu, Z.F. Ren, H.Q. Zhou, Recent developments in earth-abundant and non-noble electrocatalysts for water electrolysis, Mater. Today Phys. 7 (2018) 121–138, doi:10.1016/j.mtphys.2018.11.007.
[11] M.S. Faber, S. Jin, Earth-abundant inorganic electrocatalysts and their nanostructures for energy conversion applications, Energy Environ. Sci. 7 (2014) 3519–3542, doi:10.1039/C4EE01760A.
[12] J. Huang, Y. Sun, X. Du, Y. Zhang, C. Wu, C. Yan, Y. Yan, G. Zou, W. Wu, R. Lu, Y. Li, J. Xiong, Cytomembrane-structure-inspired active Ni-N-O interface for enhanced oxygen evolution reaction, Adv. Mater. 30 (2018) 1803367, doi:10.1002/adma.201803367.
[13] J. Sun, F. Tian, F. Yu, Z. Yang, B. Yu, S. Chen, Z. Ren, H. Zhou, Robust hydrogen-evolving electrocatalyst from heterogeneous molybdenum disulfide-based catalyst, ACS Catal 10 (2020) 1511–1519, doi:10.1021/acscatal.9b03030.
[14] Y. Yang, Y. Qian, H. Li, Z. Zhang, Y. Mu, D. Do, B. Zhou, J. Dong, W. Yan, Y. Qin, L. Fang, R. Feng, J. Zhou, P. Zhang, J. Dong, G. Yu, Y. Liu, X. Zhang, X. Fan, O-coordinated W-Mo dual-atom catalyst for pH-universal electrocatalytic hydrogen evolution, Sci. Adv. 6 (2020) eaba6586, doi:10.1126/sciadv.aba6586.
[15] J. Sun, M. Ren, L. Yu, Z. Yang, L. Xie, F. Tian, Y. Yu, Z. Ren, S. Chen, H. Zhou, Highly efficient hydrogen evolution from a mesoporous hybrid of nickel phosphide nanoparticles anchored on cobalt phosphosulfide/phosphide nanosheet arrays, Small 15 (2019) 1804272, doi:10.1002/smll.201804272.
[16] S. Song, L. Yu, X. Xiao, Z. Qin, W. Zhang, D. Wang, J. Bao, H. Zhou, Q. Zhang, S. Chen, Z. Ren, Outstanding oxygen evolution reaction performance of nickel iron selenide/stainless steel mat for water electrolysis, Mater. Today Phys. 13 (2020) 100216, doi:10.1016/j.mtphys.2020.100216.
[17] I.K. Mishra, H. Zhou, J. Sun, F. Qin, K. Dahal, J. Bao, S. Chen, Z. Ren, Hierarchical CoP/Ni_5P_4/CoP microsheet arrays as a robust pH-universal electrocatalyst for efficient hydrogen generation, Energy Environ. Sci. 11 (2018) 2246–2252, doi:10.1039/C8EE01270A.
[18] Y. Yang, H. Yao, Z. Yu, S.M. Islam, H. He, M. Yuan, Y. Yue, K. Xu, W. Hao, G. Sun, H. Li, S. Ma, P. Zapol, M.G. Kanatzidis, Hierarchical nanoassembly of MoS_2/Co_9S_8/Ni_3S_2/Ni as a highly efficient electrocatalyst for overall water splitting in a wide pH range, J. Am. Chem. Soc. 141 (2019) 10417–10430, doi:10.1021/jacs.9b04492.
[19] F. Lv, J. Feng, K. Wang, Z. Dou, W. Zhang, J. Zhou, C. Yang, M. Luo, Y. Yang, Y. Li, P. Gao, S. Guo, Iridium-tungsten alloy nanodendrites as ph-universal water-splitting electrocatalysts, ACS Cent. Sci. 4 (2018) 1244–1252, doi:10.1021/acscentsci.8b00426.
[20] X. Xiao, X. Wang, B. Li, X. Jiang, Y. Zhang, M. Li, S. Song, S. Chen, M. Wang, Y. Shen, Z. Ren, Regulating the electronic configuration of ruthenium nanoparticles via coupling cobalt phosphide for hydrogen evolution in alkaline media, Mater. Today Phys. 12 (2020) 100182, doi:10.1016/j.mtphys.2020.100182.
[21] H. Jin, J. Wang, D. Su, Z. Wei, Z. Pang, Y. Wang, In situ cobalt-cobalt oxide/n-doped carbon hybrids as superior bifunctional electrocatalysts for hydrogen and oxygen evolution, J. Am. Chem. Soc. 137 (2015) 2688–2694, doi:10.1021/ja5127165.
[22] Are metal chalcogenides, nitrides, and phosphides oxygen evolution catalysts or bifunctional catalysts, ACS Energy Lett. 2 (2017) 1937–1938, doi:10.1021/acsenergylett.7b00679.
[23] Y. Tan, H. Wang, P. Liu, Y. Shen, C. Cheng, A. Hirata, T. Fujita, Z. Tang, M. Chen, Versatile nanoporous bimetallic phosphides towards electrochemical water splitting, Energy Environ. Sci. 9 (2016) 2257–2261, doi:10.1039/C6EE01109H.
[24] L. Yan, L. Cao, P. Dai, X. Gu, D. Liu, L. Li, Y. Wang, X. Zhao, Metal-organic frameworks derived nanotube of nickel-cobalt bimetal phosphides as highly efficient electrocatalysts for overall water splitting, Adv. Funct. Mater. 27 (2017) 1703455, doi:10.1002/adfm.201703455.
[25] Y. Feng, X.-Y. Yu, U. Paik, Nickel cobalt phosphides quasi-hollow nanocubes as an efficient electrocatalyst for hydrogen evolution in alkaline solution, Chem. Commun. 52 (2016) 1633–1636, doi:10.1039/C5CC08991C.
[26] D.-H. Ha, B. Han, M. Risch, L. Giordano, K.P.C. Yao, P. Karayaylali, Y. Shao-Horn, Activity and stability of cobalt phosphides for hydrogen evolution upon water splitting, Nano Energy 29 (2016) 37–45, doi:10.1016/j.nanoen.2016.04.034.
[27] H. Du, R.-M. Kong, X. Guo, F. Qu, J. Li, Recent progress in transition metal phosphides with enhanced electrocatalysis for hydrogen evolution, Nanoscale 10 (2018) 21617–21624, doi:10.1039/C8NR07891B.
[28] S.-S. Lu, L.-M. Zhang, Y.-W. Dong, J.-Q. Zhang, X.-T. Yan, D.-F. Sun, X. Shang, J.-Q. Chi, Y.-M. Chai, B. Dong, Tungsten-doped Ni-Co phosphides with multiple catalytic sites as efficient electrocatalysts for overall water splitting, J. Mater. Chem. A 7 (2019) 16859–16866, doi:10.1039/C9TA03944A.
[29] J. Xie, Y. Xie, Transition metal nitrides for electrocatalytic energy conversion: opportunities and challenges, Chemistry 22 (2016) 3588–3598, doi:10.1002/chem.201501120.
[30] Y. Abghoui, E. Skúlason, Hydrogen Evolution reaction catalyzed by transition-metal nitrides, J. Phys. Chem. C 121 (2017) 24036–24045, doi:10.1021/acs.jpcc.7b06811.
[31] L. Yu, S. Song, B. McElhenny, F. Ding, D. Luo, Y. Yu, S. Chen, Z. Ren, A universal synthesis strategy to make metal nitride electrocatalysts for hydrogen evolution reaction, J. Mater. Chem. A 7 (2019) 19728–19732, doi:10.1039/C9TA05455C.
[32] M.-S. Balogun, Y. Huang, W. Qiu, H. Yang, H. Ji, Y. Tong, Updates on the development of nanostructured transition metal nitrides for electrochemical energy storage and water splitting, Mater. Today 20 (2017) 425–451, doi:10.1016/j.mattod.2017.03.019.
[33] H. Jin, Q. Gu, B. Chen, C. Tang, Y. Zheng, H. Zhang, M. Jaroniec, S.-Z. Qiao, Molten salt-directed catalytic synthesis of 2D layered transition-metal nitrides for efficient hydrogen evolution, Chem 6 (2020) 2382–2394, doi:10.1016/j.chempr.2020.06.037.
[34] J. Bonde, P.G. Moses, T.F. Jaramillo, J.K. Nørskov, I. Chorkendorff, Hydrogen evolution on nano-particulate transition metal sulfides, Faraday Discuss. 140 (2009) 219–231, doi:10.1039/B803857K.
[35] Y. Sun, C. Huang, J. Shen, Y. Zhong, J. Ning, Y. Hu, One-step construction of a transition-metal surface decorated with metal sulfide nanoparticles: A high-efficiency electrocatalyst for hydrogen generation, J. Colloid Interface Sci. 558 (2020) 1–8, doi:10.1016/j.jcis.2019.09.090.
[36] Y. Guo, T. Park, J.W. Yi, J. Henzie, J. Kim, Z. Wang, B. Jiang, Y. Bando, Y. Sugahara, J. Tang, Y. Yamauchi, Nanoarchitectonics for transition-metal-sulfide-based electrocatalysts for water splitting, Adv. Mater. 31 (2019) 1807134, doi:10.1002/adma.201807134.
[37] H. Li, S. Chen, Y. Zhang, Q. Zhang, X. Jia, Q. Zhang, L. Gu, X. Sun, L. Song, X. Wang, Systematic design of superaerophobic nanotube-array electrode comprised of transition-metal sulfides for overall water splitting, Nat. Commun. 9 (2018) 2452, doi:10.1038/s41467-018-04888-0.
[38] C. Huang, S. Cheng, L. Yu, W. Zhang, J. Zhou, Y. Zhang, Y. Yu, Electrolyzer with hierarchical transition metal sulfide and phosphide towards overall water splitting, Mater. Today Phys. 11 (2019) 100162, doi:10.1016/j.mtphys.2019.100162.
[39] R. Zhang, X. Wang, S. Yu, T. Wen, X. Zhu, F. Yang, X. Sun, X. Wang, W. Hu, Ternary $NiCo_2P_x$ nanowires as pH-universal electrocatalysts for highly efficient hydrogen evolution reaction, Adv. Mater. 29 (2017) 1605502, doi:10.1002/adma.201605502.
[40] X. Zhang, F. Zhou, W. Pan, Y. Liang, R. Wang, General construction of molybdenum-based nanowire arrays for pH-universal hydrogen evolution electrocatalysis, Adv. Funct. Mater. 28 (2018) 1804600, doi:10.1002/adfm.201804600.
[41] Y. Men, P. Li, F. Yang, G. Cheng, S. Chen, W. Luo, Nitrogen-doped CoP as robust electrocatalyst for high-efficiency pH-universal hydrogen evolution reaction, Appl. Catal. B 253 (2019) 21–27, doi:10.1016/j.apcatb.2019.04.038.
[42] X. Lu, T. Liu, T. Zhai, G. Wang, M. Yu, S. Xie, Y. Ling, C. Liang, Y. Tong, Y. Li, Improving the cycling stability of metal-nitride supercapacitor electrodes with a thin carbon shell, Adv. Energy Mater. 4 (2014) 1300994, doi:10.1002/aenm.201300994.
[43] X. Lu, M. Yu, T. Zhai, G. Wang, S. Xie, T. Liu, C. Liang, Y. Tong, Y. Li, High energy density asymmetric quasi-solid-state supercapacitor based on porous vanadium nitride nanowire anode, Nano Lett 13 (2013) 2628–2633, doi:10.1021/nl400760a.
[44] W.-F. Chen, J.T. Muckerman, E. Fujita, Recent developments in transition metal carbides and nitrides as hydrogen evolution electrocatalysts, Chem. Commun. 49 (2013) 8896–8909, doi:10.1039/C3CC44076A.
[45] A.-M. Alexander, J.S.J. Hargreaves, Alternative catalytic materials: carbides, nitrides, phosphides and amorphous boron alloys, Chem. Soc. Rev. 39 (2010) 4388–4401, doi:10.1039/B916787K.
[46] S.H. Gage, B.G. Trewyn, C.V. Ciobanu, S. Pylypenko, R.M. Richards, Synthetic advancements and catalytic applications of nickel nitride, Catal. Sci. Technol. 6 (2016) 4059–4076, doi:10.1039/C6CY00712K.
[47] Y. Hu, T. Xiong, M.S.J.T. Balogun, Y. Huang, D. Adekoya, S. Zhang, Y. Tong, Enhanced metallicity boosts hydrogen evolution capability of dual-bimetallic Ni-Fe nitride nanoparticles, Mater. Today Phys. 15 (2020) 100267, doi:10.1016/j.mtphys.2020.100267.
[48] W. Sun, W. Wei, N. Chen, L. Chen, Y. Xu, C.J. Oluigbo, Z. Jiang, Z. Yan, J. Xie, In situ confined vertical growth of a 1D-$CuCo_2S_4$ nanoarray on Ni foam covered by a 3D-PANI mesh layer to form a self-supporting hierarchical structure for high-efficiency oxygen evolution catalysis, Nanoscale 11 (2019) 12326–12336, doi:10.1039/C9NR02815C.
[49] Q. Han, Z. Cheng, J. Gao, Y. Zhao, Z. Zhang, L. Dai, L. Qu, Mesh-on-mesh graphitic-C_3N_4@graphene for highly efficient hydrogen evolution, Adv. Funct. Mater. 27 (2017) 1606352, doi:10.1002/adfm.201606352.
[50] D. Kong, H. Wang, Z. Lu, Y. Cui, $CoSe_2$ nanoparticles grown on carbon fiber paper: an efficient and stable electrocatalyst for hydrogen evolution reaction, J. Am. Chem. Soc. 136 (2014) 4897–4900, doi:10.1021/ja501497n.
[51] X. Zhang, S. Liu, Y. Zang, R. Liu, G. Liu, G. Wang, Y. Zhang, H. Zhang, H. Zhao, Co/Co_9S_8@S,N-doped porous graphene sheets derived from S, N dual organic ligands assembled Co-MOFs as superior electrocatalysts for full water splitting in alkaline media, Nano Energy 30 (2016) 93–102, doi:10.1016/j.nanoen.2016.09.040.
[52] Y. Li, F. Cheng, J. Zhang, Z. Chen, Q. Xu, S. Guo, Cobalt-Carbon core-shell nanoparticles aligned on wrinkle of N-doped carbon nanosheets with Pt-like activity for oxygen reduction, Small 12 (2016) 2839–2845, doi:10.1002/smll.201600336.
[53] T. Higashi, H. Nishiyama, Y. Otsuka, Y. Kawase, Y. Sasaki, M. Nakabayashi, M. Katayama, T. Minegishi, N. Shibata, K. Takanabe, T. Yamada, K. Domen, Efficient water oxidation using Ta_3N_5 thin film photoelectrodes prepared on insulating transparent substrates, ChemSusChem 13 (2020) 1974–1978, doi:10.1002/cssc.202000397.
[54] W. Zhou, Y. Zhou, L. Yang, J. Huang, Y. Ke, K. Zhou, L. Li, S. Chen, N-doped carbon-coated cobalt nanorod arrays supported on a titanium mesh as highly active electrocatalysts for the hydrogen evolution reaction, J. Mater. Chem. A 3 (2015) 1915–1919, doi:10.1039/C4TA06284A.

[55] J. Cui, T. Liu, B. Dong, Y. Qi, H. Yuan, J. Gao, D. Yang, F. Zhang, Flux-assisted synthesis of prism-like octahedral Ta_3N_5 single-crystals with controllable facets for promoted photocatalytic H2 evolution, Solar RRL (2020) n/a2000574., doi:10.1002/solr.202000574.
[56] Z. Luo, C. Cong, J. Zhang, Q. Xiong, T. Yu, The origin of sub-bands in the Raman D-band of graphene, Carbon 50 (2012) 4252–4258, doi:10.1016/j.carbon.2012.05.008.
[57] W.-H. Hu, G.-Q. Han, Y.-R. Liu, B. Dong, Y.-M. Chai, Y.-Q. Liu, C.-G. Liu, Ultrathin MoS_2-coated carbon nanospheres as highly efficient electrocatalyts for hydrogen evolution reaction, Int. J. Hydrog. Energy 40 (2015) 6552–6558, doi:10.1016/j.ijhydene.2015.03.150.
[58] W.-J. Chun, A. Ishikawa, H. Fujisawa, T. Takata, J.N. Kondo, M. Hara, M. Kawai, Y. Matsumoto, K. Domen, Conduction and valence band positions of Ta_2O_5, TaON, and Ta_3N_5 by UPS and electrochemical methods, J. Phys. Chem. B 107 (2003) 1798–1803, doi:10.1021/jp027593f.
[59] Y. Li, T. Takata, D. Cha, K. Takanabe, T. Minegishi, J. Kubota, K. Domen, Vertically aligned Ta_3N_5 nanorod arrays for solar-driven photoelectrochemical water splitting, Adv. Mater. 25 (2013) 125–131, doi:10.1002/adma.201202582.
[60] Z. Li, M. Shao, L. Zhou, R. Zhang, C. Zhang, M. Wei, D.G. Evans, X. Duan, Directed growth of metal-organic frameworks and their derived carbon-based network for efficient electrocatalytic oxygen reduction, Adv. Mater. 28 (2016) 2337–2344, doi:10.1002/adma.201505086.
[61] T. Higashi, H. Nishiyama, Y. Suzuki, Y. Sasaki, T. Hisatomi, M. Katayama, T. Minegishi, K. Seki, T. Yamada, K. Domen, Transparent Ta_3N_5 photoanodes for efficient oxygen evolution toward the development of tandem cells, Angew. Chem. Int. Ed. 58 (2019) 2300–2304, doi:10.1002/anie.201812081.
[62] D.-W. Wang, D. Su, Heterogeneous nanocarbon materials for oxygen reduction reaction, Energy Environ. Sci. 7 (2014) 576–591, doi:10.1039/C3EE43463J.
[63] Z. Wu, L.-P. Sun, M. Yang, L.-H. Huo, H. Zhao, J.-C. Grenier, Facile synthesis and excellent electrochemical performance of reduced graphene oxide-Co_3O_4 yolk-shell nanocages as a catalyst for oxygen evolution reaction, J. Mater. Chem. A 4 (2016) 13534–13542, doi:10.1039/C6TA04943E.
[64] H. Wang, S. Min, C. Ma, Z. Liu, W. Zhang, Q. Wang, D. Li, Y. Li, S. Turner, Y. Han, H. Zhu, E. Abou-hamad, M.N. Hedhili, J. Pan, W. Yu, K.-W. Huang, L.-J. Li, J. Yuan, M. Antonietti, T. Wu, Synthesis of single-crystal-like nanoporous carbon membranes and their application in overall water splitting, Nat. Commun. 8 (2017) 13592, doi:10.1038/ncomms13592.
[65] Y. Li, H. Wang, L. Xie, Y. Liang, G. Hong, H. Dai, MoS_2 Nanoparticles grown on graphene: an advanced catalyst for the hydrogen evolution reaction, J. Am. Chem. Soc. 133 (2011) 7296–7299, doi:10.1021/ja201269b.
[66] I.K. Mishra, H. Zhou, J. Sun, K. Dahal, Z. Ren, R. He, S. Chen, Z. Ren, Highly efficient hydrogen evolution by self-standing nickel phosphide-based hybrid nanosheet arrays electrocatalyst, Mater. Today Phys. 4 (2018) 1–6, doi:10.1016/j.mtphys.2018.01.001.